JMEPEG (2015) 24:3919–3932
DOI: 10.1007/s11665-015-1680-1

1059-9495/$19.00

Prediction of Phase Transformation and Hardness Distribution of AISI 1045 Steel After Spot Continual Induction Hardening

Shengxiao Zhu, Zhou Wang, Xunpeng Qin, Huajie Mao, and Kai Gao

(Submitted December 10, 2014; in revised form June 18, 2015; published online September 1, 2015)

An numerical and experimental study of spot continual induction hardening (SCIH) for AISI 1045 steel was carried out to gain a better understanding of this non-stationary and transverse flux induction hardening treatment. The SCIH device was set up by assembling the single-turn coil inductor to a five-axis cooperating computer numerical control system. The influence of inductor velocity, input current, and quenching medium on temperature field was estimated via the SCIH model, and the simulated micro-hardness and microstructure were validated by experimental verification. The heating delay phenomenon appearing in the SCIH process had been analyzed.

Keywords AISI 1045 steel, heating delay phenomenon, quenching medium, spot continual induction hardening (SCIH)

1. Introduction

Induction hardening is frequently preformed in order to form a surface layer of martensitic in specific areas of the work piece. This hardening method can improve mechanical properties of metal component without affecting the remainder of the part. It is a clean and efficient surface hardening process with many advantages such as fast heating rate, good reproducibility, well-distributed hardness, and low energy consumption (Ref 1, 2). The typical procedure for induction hardening involves heating the component to the austenitizing temperature range, holding it at a temperature long enough for complete austenitizing, and then rapidly cooling the alloy until it is below the Ms temperature. As more and more complicated components are used in equipment manufacturing industry, the conventional induction hardening method cannot meet the requirement of the hardening process for specific components. Many modified induction hardening methods including spot induction hardening (SIH) method have been proposed in the last two decades (Ref 3, 4). The aim of all these works is to make the induction hardening method more efficient and deal with some complicated or specific components. For example, SIH method, which combines the advantages of surface induction hardening and selective hardening, can realize a small region heat treatment on curved surface or some other complicated component. The most interesting design in SIH is the inductor, which uses a magnetizer installed on a small single-turn coil with the aim of increasing the heat efficiency of the inductor. Compared with longitudinal flux induction heating, the transverse flux heating using in SIH method is more efficient and can harden very small area because of the novel inductor (Ref 4, 5). However, the main shortcoming of SIH method is lack of flexibility if more than one small area or relative large area needs to be hardened. The first task of this work is to increase the flexibility of SIH process. A single-turn coil inductor is assembled to a five-axis cooperating computer numerical control (CNC) system with the aim of precise control of inductor movement. This new induction hardening method is called spot continual induction hardening (SCIH) method. The second task of this work is to model the SCIH process by commercial code ANSYS finite element package. It is clear that the induction hardening is a complex combination of electromagnetic, heat transfer, and metallurgical phenomena. Modeling this process is difficult because the temperature and electromagnetic fields as well as phase transformation are needed to be coupled in the FEM model. Furthermore, as the inductor moves during SCIH process, the relative position of inductor and treated workpiece always changes in SCIH process. The SCIH process belongs to continual induction hardening treatment. The simulation of SCIH process involves not only the non-liner coupled problem of temperature, electromagnetic fields and phase transformation but also the non-stationary problem with time-dependent boundary conditions.

The simulation of static and continual induction hardening is not new, and many researchers have done some valuable works about this issue. A broad overview of induction hardening simulation can be found in the work of Rudnev and loveless (Ref 6, 7). They did a lot of experimental and numerical work about induction hardening and compared the advantages and disadvantages of different numerical method in induction hardening simulation recently (Ref 7). Montalvo-Urquizo et al. (Ref 8) investigated a thermo-mechanical model for

Shengxiao Zhu and **Huajie Mao**, School of Materials Science and Engineering, Wuhan University of Technology, Wuhan 430070, Hubei, China and Hubei Key Laboratory of Advanced Technology for Automotive Components, Wuhan 430070, Hubei, China; and **Zhou Wang**, **Xunpeng Qin**, and **Kai Gao**, School of automotive Engineering, Wuhan University of Technology, Wuhan 430070, Hubei, China and Hubei Key Laboratory of Advanced Technology for Automotive Components, Wuhan 430070, Hubei, China. Contact e-mails: 774175507@qq.com and wangzhou@whut.edu.cn.

induction hardening of 42CrMo4 steel. The model accounts for the thermo-mechanical effects coupled with phase transitions during the induction hardening. A comparison concerning the effect of transformation induced plastic strain (TRIP) was carried out in the proposed model and showed the consideration of TRIP produced significant differences in stress results and could not be neglected in their model. The simulation was very creative but not verified by experiment. Magnabosco et al. (Ref 9) investigated the induction hardening process of type C45 steel experimentally and numerically. The proposed model in their work was used to simulate the heat treatment in order to predict the thermal history, the phase distributions, and the micro-hardness profiles. The simulated and the experimental results agreed well with each other, though there were many undefined hypothesis existing in their work, and the simulated model was simplified to 2D. Doležel et al. (Ref 10) proposed a continual surface induction hardening model for a moving cylindrical inductor. The convective coefficient in the model was defined by means of a special theoretically empirical algorithm and the division of the heated body into more parts in continual induction hardening process would improve the accuracy of the simulated results. Karban et al. (Ref 11) proposed a slightly simplified mathematical model that used the Helmholtz equation for the description of electromagnetic field and non-stationary heat transfer equation of continual induction hardening process. The boundary conditions in continual induction hardening varied with time and were adjusted at every time step. An algorithm of modeling continual induction hardening was proposed by two virtual examples but lack of experimental verification. Gao et al. (Ref 4) proposed an electromagnetic model coupled temperature fields with time-dependent boundary conditions for spot induction hardening process. The phenomenology model in their work presented a novel and simplified way to predict the temperature, the hardness, and phase transformation in spot induction hardening process even with an inadequate material model. Besides, the induction hardening model was static and the inductor did not move in their work.

Therefore, in the present work, experimental and numerical investigations on SCIH process with considering electromagnetic, heat transfer, and metallurgical phenomena were carried out by self-designed SCIH equipment and commercial FEM code ANSYS. The simulation as well as the experimental results of temperature, micro-hardness, and microstructure were presented and discussed.

2. Experiment Setup

Figure 1 shows the system of self-designed SCIH equipment. A single-turn copper coil is assembled to a five-axis cooperating CNC machine tools to realize a small region induction hardening of complicated component surface. During SCIH process, the inductor carrying harmonic current moved with a certain velocity along the component surface, and the sprayer moved with the inductor in order to assure consequent fast cooling of the heated part. The movements of the inductor and the cooling sprayer are controlled by CNC system. The magnetizer is mounted at the inductor with the aim of heightening heat efficiency in the SCIH process.

In the experimental process of SCIH, the frequency of induction heating power supply was 30 kHz and the working voltage was 380 V. The distance between induction and

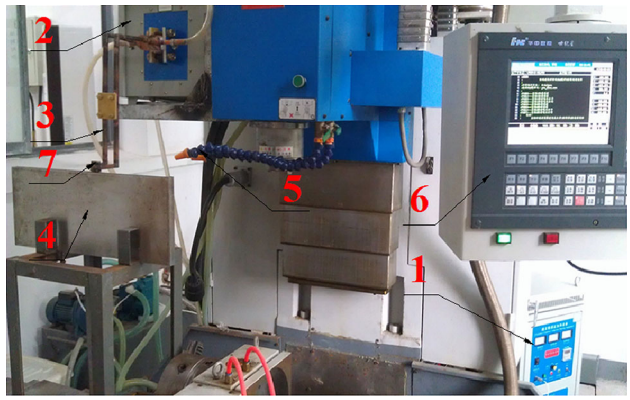

Fig. 1 The self-designed SCIH system. 1. High-frequency induction heating power supply, 2. Transformer, 3. Inductor, 4. Steel workpiece, 5. Cooling sprayer, 6. CNC system, 7. Magnetizer

workpiece was 2 mm, and the current value of inductor (I) can be calculated by input current value I_0 according to the practical circuit diagram (Ref 4):

$$I = \frac{I_0 \times n \times (1 - \eta_1)}{N \times \alpha\eta_2}, \quad \text{(Eq 1)}$$

where I_0 is input current, n is turns ratio between primary coil and the secondary coil in transformer, η_1 is the loss of transformer, N is turns ratio of inductor, α is power factor of the system, and η_2 is efficiency of transformation between primary coil and the secondary coil. The current used in the numerical simulation is calculated according to the current value of inductor by the Eq 1.

3. Mathematical Model of SCIH

3.1 Electromagnetic and Temperature Field

The distribution of electromagnetic field equation is partial differential equation, and the mutual interaction of the nonlinear electromagnetic and non-stationary temperature fields with time-dependent boundary conditions exists during SCIH process. The global system of equations modeling electromagnetic field is based on the four Maxwell equations:

$$\nabla \times \boldsymbol{H} = \boldsymbol{J}, \quad \text{(Eq 2)}$$

$$\nabla \times \boldsymbol{E} = -\frac{\partial \boldsymbol{B}}{\partial \boldsymbol{t}}, \quad \text{(Eq 3)}$$

$$\nabla \times \boldsymbol{D} = 0, \quad \text{(Eq 4)}$$

$$\nabla \times \boldsymbol{B} = 0, \quad \text{(Eq 5)}$$

where $\boldsymbol{B}$ is the magnetic flux density vector, $\boldsymbol{H}$ is the strength of the magnetic field vector, $\boldsymbol{E}$ is the electric field intensity vector, $\boldsymbol{J}$ is the conduction current vector, $\nabla = (\partial/\partial \boldsymbol{x}, \partial/\partial \boldsymbol{y}, \partial/\partial \boldsymbol{z})$, and $\times$ denotes the vector product.

According to Stratton (Ref 12) and Karban et al.'s (Ref 11) investigation, the distribution of electromagnetic field is generally described by equation

$$\nabla \times \frac{1}{\mu} \nabla \times \boldsymbol{A} + \gamma \frac{\partial \boldsymbol{A}}{\partial \boldsymbol{t}} = \gamma \boldsymbol{v} \times \boldsymbol{A} + \boldsymbol{J}_s, \quad \text{(Eq 6)}$$

where A denotes the magnetic vector potential, μ is the magnetic permeability, γ is the electrical conductivity, t is time, J_s is the uniform density of the field current in the inductor, and v is the velocity of inductor.

The purpose of calculating the electromagnetic field and eddy current field is to get the Joule heat to estimate the temperature field. The boundary condition of temperature field should be set up according to the heating and quenching process. The heat losses from the heated workpiece to the ambient medium are generally caused by convection and radiation. Compared with the heat loss of convection, the heat loss of radiation can be neglected because the amount of radiation heat loss in SCIH process is very small (Ref 11). Therefore, the thermal boundary condition in the model can be expressed by

$$-\frac{\partial T}{\partial n} = h(T_w - T_{cm}), \quad \text{(Eq 7)}$$

where h denotes the heat transfer coefficient, T_w (K) is the surface temperature of workpiece, and T_{cm} (K) is the temperature of the ambient cooling medium. 20 °C is set for ambient temperature. In this model, the heat transfer coefficient of cooling water is 10000 W/(m^{2}K), the oil convection coefficient is 2000 W/(m^{2}K), and the air convection coefficient is 10 W/(m^{2}K) (Ref 3, 4).

3.2 Microstructure Transformation

The workpiece in this work was AISI 1045 steel normalized at 850 °C. The chemical composition was 0.46C, 0.27Si, 0.74Mn, 0.2Ni, 0.15Cr, 0.021S, 0.014P, and the rest Fe (all in wt.%). The initiating and completing austenite transformation temperatures (AC1 and AC3) of the AISI 1045 steel were 740 and 800 °C, respectively, according to the iron-carbon diagram.

In order to describe the different types of phase transformation and micro-hardness of AISI 1045 steel treated by SCIH process, a continuous cooling transformation (CCT) phase curve of AISI 1045 steel was carried out in the microstructure transformation model, which is depicted in Fig. 2 (Ref 13).

It can be seen from the CCT curve of 1045 steel that different cooling rates lead to different phase transformations. The Eq 8-10 given by Magnabosco et al. (Ref 9) show the calculation of micro-hardness by taking into account of the material chemical composition, the final microstructure, and the cooling rate at 700 °C (v_R) while neglecting the grain size effect on micro-hardness. According to the nominal chemical composition of the workpiece presented above, Eq 8 can be simplified to Eq 11.

$$\mathrm{HV}_{\mathrm{martensite}} = 127 + 947\mathrm{C} + 27\mathrm{Si} + 11\mathrm{Mn} + 8\mathrm{Ni} + 16\mathrm{Cr} + 21\mathrm{Log}_{10}V_R, \quad \text{(Eq 8)}$$

$$\mathrm{HV}_{\mathrm{bainite}} = -323 + 185\mathrm{C} + 330\mathrm{Si} + 153\mathrm{Mn} + 65\mathrm{Ni} + 144\mathrm{Cr} + 191\mathrm{Mo} + \mathrm{Log}_{10}V_R \times (89 + 53\mathrm{C} - 55\mathrm{Si} - 22\mathrm{Mn} - 10\mathrm{Ni} - 20\mathrm{Cr} - 33\mathrm{Mo}) \quad \text{(Eq 9)}$$

$$HV_{\mathrm{ferrite}} = 42 + 223\mathrm{C} + 53\mathrm{Si} + 30\mathrm{Mn} + 12.6\mathrm{Ni} + 7\mathrm{Cr} + 1\mathrm{Mo} + \mathrm{Log}_{10}V_R \times (10 - 19\mathrm{Si} + 4\mathrm{Ni} + 8\mathrm{Cr} + 130V), \quad \text{(Eq 10)}$$

$$HV_{\mathrm{martensite}} = 582.05 + 21\mathrm{Log}_{10}V_R. \quad \text{(Eq 11)}$$

According to the CCT diagram shown in Fig. 2, if 100% austenitic transformation is completed, 100% martensite structure can be obtained when the cooling rate is more than 200 °C/s, 100% pearlite structure can be obtained when the cooling rate is less than 21 °C/s, and the bainite structure appears when the cooling rate is between 21 and 200 °C/s (Ref 4, 14).

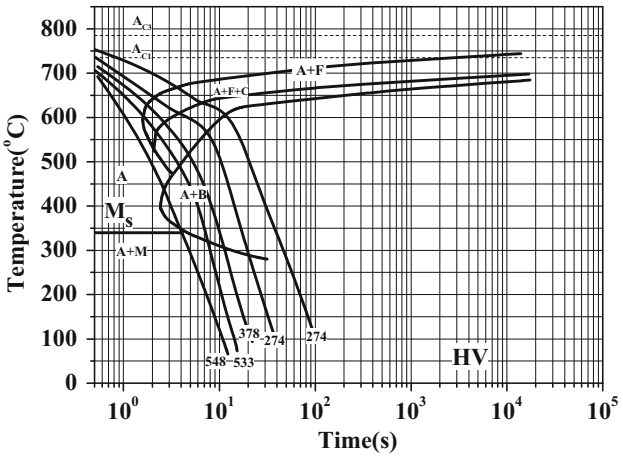

Fig. 2 The diagram of continuous cooling transformations of AISI 1045 steel

3.3 Finite Element Modeling of SCIH

In SCIH model, the temperature-related material properties such as the relative permeability, resistivity, thermal conductivity, and specific heat of AISI 1045 steel are depicted in Fig. 3 (Ref 4).

The schematic FE model of SCIH process built by ANSYS (13.0) software is depicted in Fig. 4. The dimensions of the workpiece (L × W × H) were 300 mm × 100 mm × 20 mm. The dimensions of cross section of U-type inductor were 10 mm × 10 mm, and wall thickness was 1 mm. The length and the height of U-type inductor were 40 and 50 mm, respectively. The dimensions of the magnetizer (L × W × H) were 20 mm × 20 mm × 15 mm.

The hexahedron mesh was generated in the workpiece, and the tetrahedral mesh was generated in the air, U-type inductor, and magnetizer shown in Fig. 4. The temperature gradient becomes very large in the surface layer because of the skin effect in induction hardening process. Therefore, the element of surface layer was subdivided with the aim of achieving reliable results. Specifically, the width and the length of the top surface were 2.5 mm × 5 mm, the minimum distance between nodes were 1.25 and 2.5 mm, respectively. The thickness of those element was 0.245 mm and element featured thickness increased with depth. According to the actual experimental condition, the Z-axis freedom of bottom surface of workpiece was constrained. The number of elements of the workpiece, inductor, magnetizer, and air was 24000, 1825, 1689, and 29528, respectively.

In particular, the movement of the inductor and cooling spray are modeled by means of loop statement which can modify the heat transfer coefficient according to the position of the cooling medium load. Figure 5 shows a scheme of the SCIH process. In the SCIH process, cooling medium was loaded after 3 s and moved with the inductor step by step.

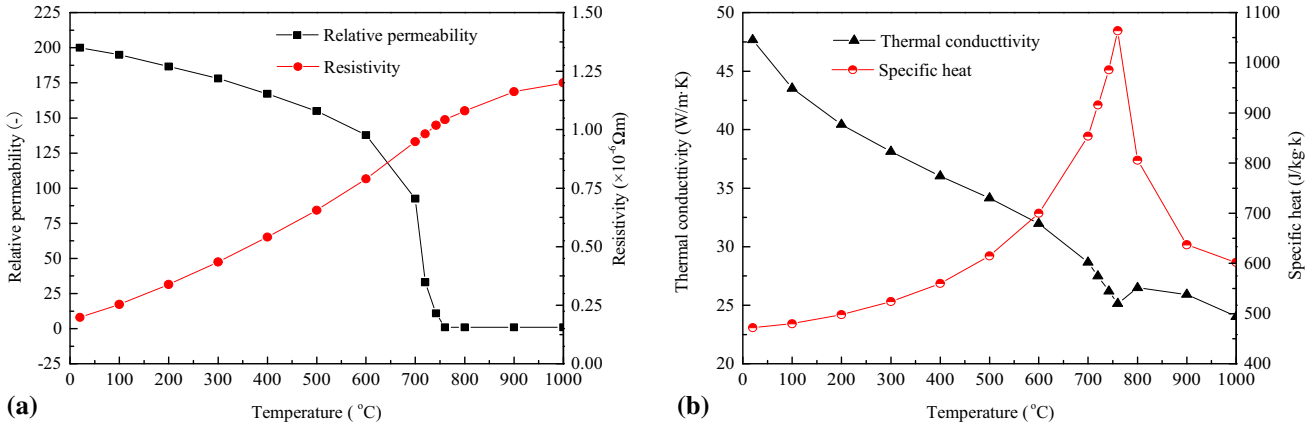

Fig. 3 The material properties with temperature variation of AISI 1045 steel, (a) Relative permeability and resistivity, (b) Thermal conductivities and specific heat

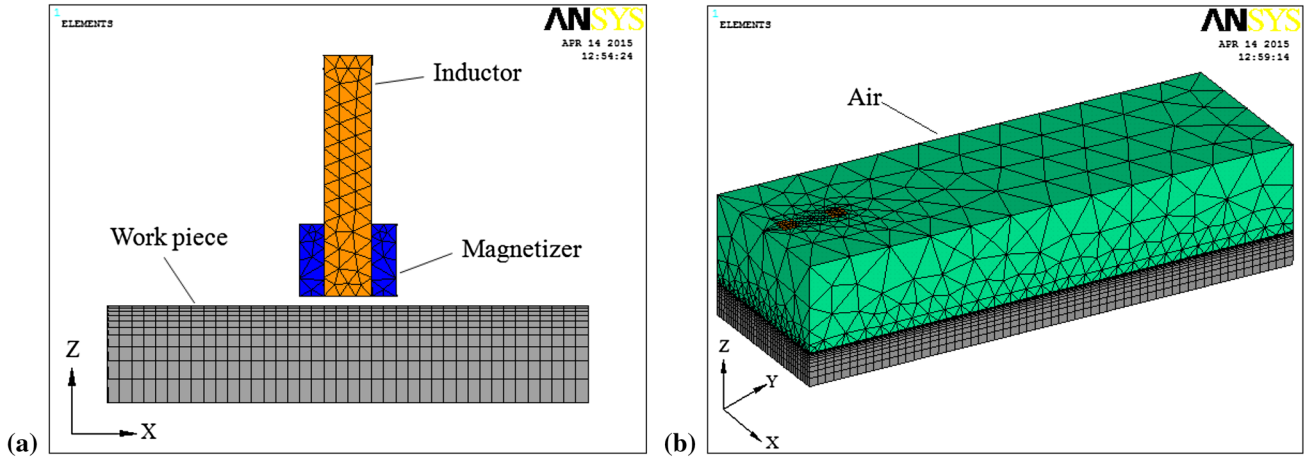

Fig. 4 (a) The FEM mesh of inductor, magnetizer and workpiece, (b) The FEM mesh of the whole model

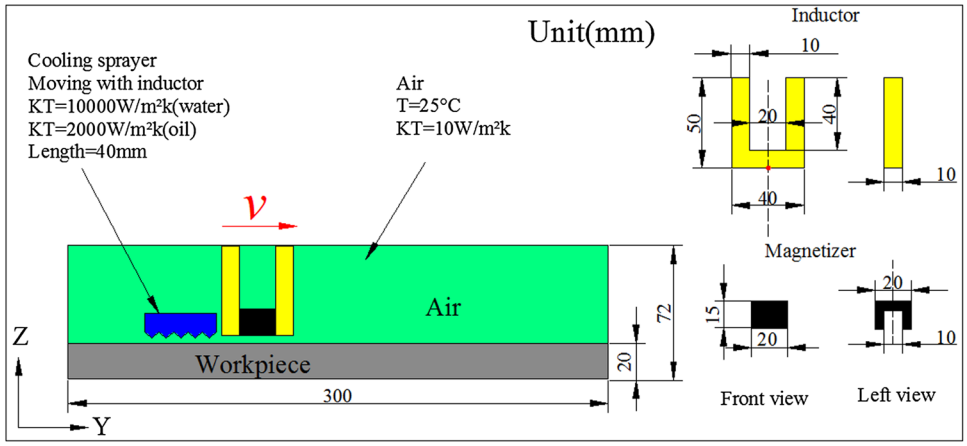

Fig. 5 Schematic diagram of the SCIH model

In the finite element simulation, electromagnetic field and temperature field analysis were coupled by indirectly method. The continual induction hardening was realized by decomposing continuous process into each transient step. In the SCIH model, the Joule heat generated by eddy current was loaded as the initial thermal boundary condition in temperature field. As

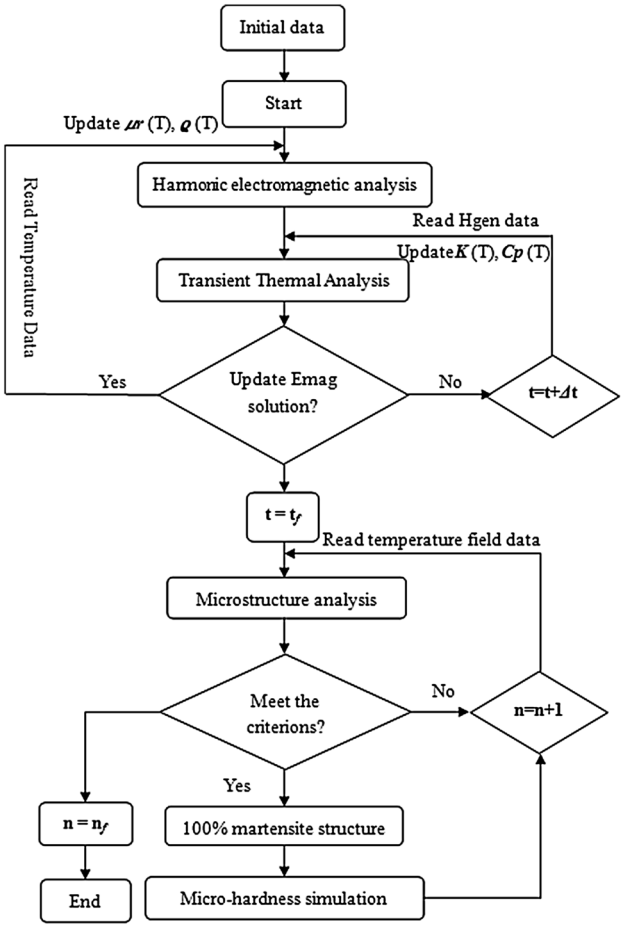

Fig. 6 The flow chart of coupling analysis

the temperature-related material properties varied with temperature variation, the new temperature-related material properties were calculated in electromagnetic field, and the data were reread in temperature field again for the next iterative step. In terms of microstructure calculation, the two criteria for phase transformation in the model were the highest heating temperature and the cooling rate. The temperature filed data of every element was read in the microstructure and micro-hardness analyses. This step determined whether the transformation of 100% martensite was completed or not in all elements of workpiece (n_f = 24000). The flow chart of coupled electromagnetic-thermal as well as microstructure analysis is depicted in Fig. 6. The simulation environment was the ANSYS (13.0) Multi-physics. The computation was performed on an Intel Xeon Dual core processor E5645 2.40 GHz personal computer workstation, and the typical CPU time was 46 to 48 h for each case.

4. Results and Discussion

4.1 Temperature Analysis

It is well known the hardness zone treated by induction hardening is directly related to temperature distribution. The temperature distribution is controlled by the SCIH parameters such as frequency, the moving velocity of inductor, the power,

Table 1 The parameters of SCIH process in simulation

Group	Input current, A	Velocity, m/s			Cooling medium	
A	1700	0.01	0.02	0.03	Oil	Water
B	1800	0.01	0.02	0.03	Oil	Water
C	1900	0.01	0.02	0.03	Oil	Water

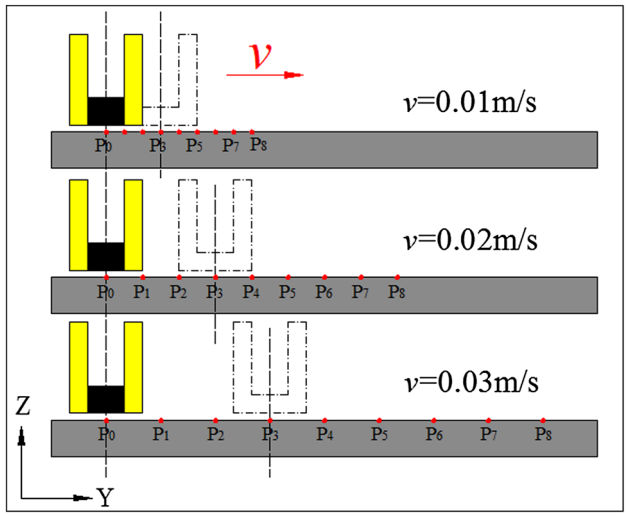

Fig. 7 The schematic diagram of the positions of observation points with different induction velocities

the quenching medium, and the geometry of workpiece and inductor. As the frequency of induction hardening power supply was 30 kHz in experiment, all input frequency in simulation was set as 30 kHz. The dimensions of workpiece and the inductor as well as magnetizer are introduced in section 3.3. In order to investigate the influence of these three kinds of parameters (input current, inductor velocity and the cooling medium) on surface hardening effect, different parameters were chosen in the numerical model. The detailed SCIH parameters are shown in Table 1.

The numerical analysis was divided into *A*, *B*, and *C* groups. Every group has the same input current. Three inductor velocities and two kinds of quenching medium were chosen in each group. For instance, A_{1w} represents the sample treated by the parameters of 1700 A, 0.01 m/s, and water cooling; B_{2O} represents the sample treated by the parameters of 1800 A, 0.02 m/s, and oil cooling.

As the rectangular workpiece was symmetric and the induction moved along the middle line of treated surface in *Y* direction, the highest temperature always appeared at the center line of the workpiece surface. In order to investigate the temperature field in SCIH process, different points on the middle line of treated surface (*XY* plane) were chosen as the observation points. The projection of inductor middle point on workpiece treated plane at its initial position was selected as the Point P0, and the distance between every observation point was calculated according to the velocity of the inductor. The observation point was numbered from the SCIH process beginning to its end, which was also shown in Fig. 7. Table 2 shows the position of observation points in the model, where *v* denotes the velocity of inductor. Figure 8 shows the temperature variation of different observation points with time in

Table 2 The positions of observation points (according to the inductor moving velocity)

Point	P0	P1	P2	P3	P4	P5	P6	P7	P8
Distance (mm)	0	v	$2v$	$3v$	$4v$	$5v$	$6v$	$7v$	$8v$
Time (s)	0	1	2	3	4	5	6	7	8

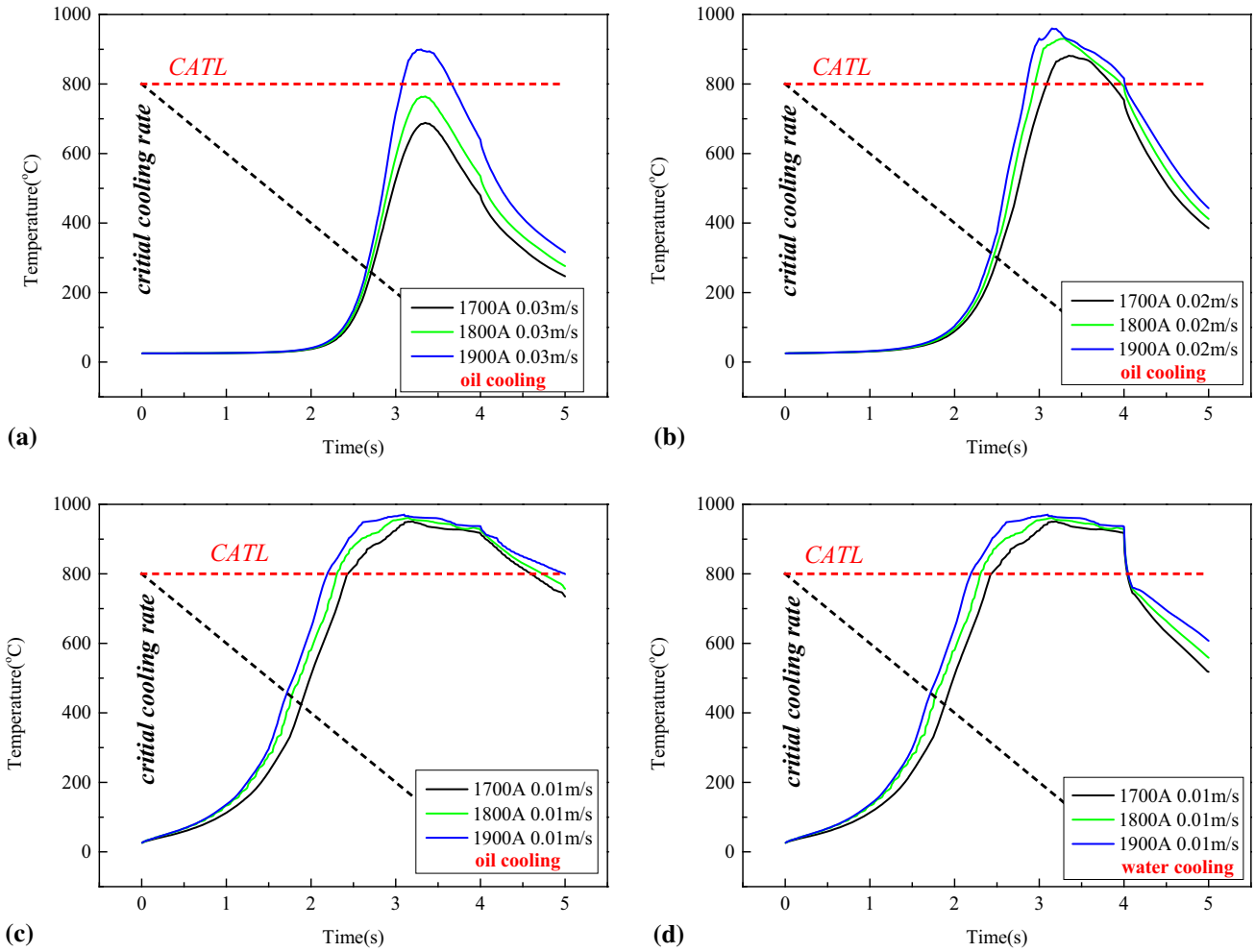

Fig. 8 Temperature-time curves of point P3 in different SCIH parameters

different conditions. The red-dotted line named CATL represents the complete austenitizing temperature line of AISI 1045 (800 °C in the model) and the black-dotted line represents the critical cooling rate for martensite transformation (200 °C/s) (Ref 14). The temperature and the cooling rate of every node in simulation would be judged by these two criteria. If the temperature is higher than 800 °C, and the cooling rate is larger than the critical cooling rate, the 100% martensite microstructure can be obtained in the simulation.

In this model, three parameters of SCIH including the input current, the moving velocity of inductor, and the cooling medium were analyzed. As the heat transfer coefficient of water is larger than that of oil, if surface hardening can be obtained with oil, the surface hardening must be obtained with water. Therefore, the SCIH modeling with cooling medium of oil was carried out first in our work. Figure 8(a-c) shows the temperature developments of point P3 with inductor moving velocity of 0.03, 0.02, and 0.01 m/s, respectively. The cooling medium is oil in these three conditions. From Fig. 8(a), it can be seen that the highest temperatures of point P3 with 1700 and 1800 A under inductor velocity of 0.03 m/s are lower than the complete austenitizing temperature, so 100% martensite microstructure cannot be obtained in these two cases. From Fig. 8(b), it can be seen that the highest temperatures of point P3 with input currents of 1700, 1800, and 1900 A are higher than the complete austenitizing temperature when inductor velocity is 0.02 m/s. In addition, all the cooling rates of point P3 are larger than the critical cooling rate of martensitic transformation. Therefore, the martensite structure can be obtained in the near surface region in the condition of inductor velocity of 0.02 m/s. From Fig. 8(c), it can be seen that even though the highest temperatures of point P3 are higher than the complete austenitizing temperature when inductor velocity is 0.01 m/s, the martensite structure cannot be obtained with oil cooling because the cooling rates are lower than

the critical cooling rate of martensitic transformation with input currents of 1700, 1800, and 1900 A. As the cooling rate by water is larger than that by oil, cooling medium of water was carried out on SCIH model. Figure 8(d) shows the temperature developments of point P3 with inductor moving velocity of 0.01 m/s under water cooling. It can be seen that all the cooling rates are larger than the critical cooling rate of martensitic transformation. Specifically, the cooling rate becomes lower with input current increasing. The cooling rate under 1900 A is nearly the same as the critical cooling rate of martensitic transformation. It is reasonable to estimate the martensitic transformation cannot occur if the input current is larger than 1900 A. Therefore, the discussion about the inductor velocity which is less or equal to 0.01 m/s will not be carried out in the following work. By comprehensive comparison of the four pictures in Fig. 8, it can be seen that the heating rate and the highest temperature become larger with the increasing of input current under the same inductor velocity. The influence of input current on the highest temperature becomes more obvious with the increasing of velocity. In order to obtain martensite microstructure on surface, large cooling rate is needed especially in the condition of high input current and low inductor velocity.

By analyzing the times of point P3 reaching their highest temperatures in different conditions shown in Fig. 8(a-c), it can be seen that this value changes with input current and inductor velocity. This phenomenon means the relative distance (RD) between P3 and the inductor middle point (Point *A* shown in Table 3) changes with the variation of input current and inductor velocity when P3 reaches its highest temperature. Table 3 shows the times of point P3 reaching its highest temperature and the value of RD in different SCIH conditions. The value of RD represents the degree of heating delay phenomenon in different conditions.

From Table 3, it can be seen that the time of point P3 reaching its highest temperature and the value of RD increase with the increasing of inductor velocity when input current stays the same; the time and the value of RD decrease with the increasing of input current when the inductor velocity keeps the same. The heating delay phenomenon appears in all induction heating conditions. Furthermore, it is clearly shown in Table 3 that this phenomenon becomes more obvious in the condition of relatively low input current (1700 A) and relatively large inductor velocity (0.03 m/s).

In order to investigate the temperature development in depth direction during different SCIH processes, different points from surface to core region were be chosen at the point P3 and the points just below P3. Figure 9(a) shows the temperature developments of different points in depth direction in the condition of 0.02 m/s, 1800 A, and oil cooling. Figure 9(b) shows the results in the condition of 0.02 m/s, 1900 A, and oil cooling. Figure 9(c) shows the results in the condition of 0.03 m/s, 1900 A, and oil cooling. Figure 9(d) shows the results in the condition of 0.03 m/s, 1900 A, and water cooling. By comparing with Fig. 9(a) and (b), it can be seen that the influence of current on the highest temperature of chosen points is obvious. The cooling rates of all points in complete austenitizing region are larger than the critical cooling rate of martensitic transformation, which represents the maximum depths of 100% martensite zone in B_{2O} and C_{2O} conditions are both in the range from depth of 0.805 and 1.12 mm. Assuming the temperature variation is linear in that area, the maximum depths of 100% martensite zone in B_{2O} and C_{2O} conditions are about 0.873 and 1.03 mm, respectively. By comparing Fig. 9(b) and (c), it can be seen that the maximum depth of complete austenitizing zone decreases with inductor velocity increasing if other conditions are same. It also can be seen from Fig. 9(c) that the cooling rates of all points in complete austenitizing region are larger than the critical cooling rate of martensitic transformation. Assuming the temperature variation is linear in depth direction, the maximum depth of 100% martensite zone is about 0.67 mm. By comparing Fig. 9(c) and (d), it can be seen that changing the quenching medium nearly does not affect the highest temperatures but affects the cooling rates of chosen points obviously. Therefore, it can be concluded that changing the cooling medium does not affect the depth of 100% martensite zone when the inductor velocity is relatively high (such as 0.03 m/s). However, when the inductor velocity is relatively low (such as 0.01 m/s), the influence of cooling medium on the depth of 100% martensite zone becomes obvious, which is because water cooling can increase the cooling rates of all chosen points significantly.

From the former simulated results, it can be seen that in the condition of 0.02 m/s, 1800 A, and water quenching medium (B_{2w}), the highest temperature of near surface region is higher than complete austenitizing temperature and the cooling rate of this region is larger than the critical cooling rate of martensitic transformation. In order to verify the SCIH model, this condition was chosen as processing parameters in SCIH experiment. Table 4 shows the parameters of SCIH in simulation and experiment.

Table 3 The time of point P3 reaching its highest temperature and the value of RD

Medium	Oil cooling								
Current(A)	1700			1800			1900		
Velocity(m/s)	0.01	0.02	0.03	0.01	0.02	0.03	0.01	0.02	0.03
Time(s)	3.20	3.35	3.36	3.15	3.30	3.35	3.10	3.15	3.30
Distance(mm)	2	7.0	10.8	1.5	6.0	10.5	1	3.0	9

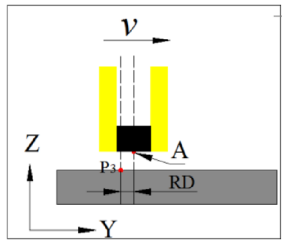

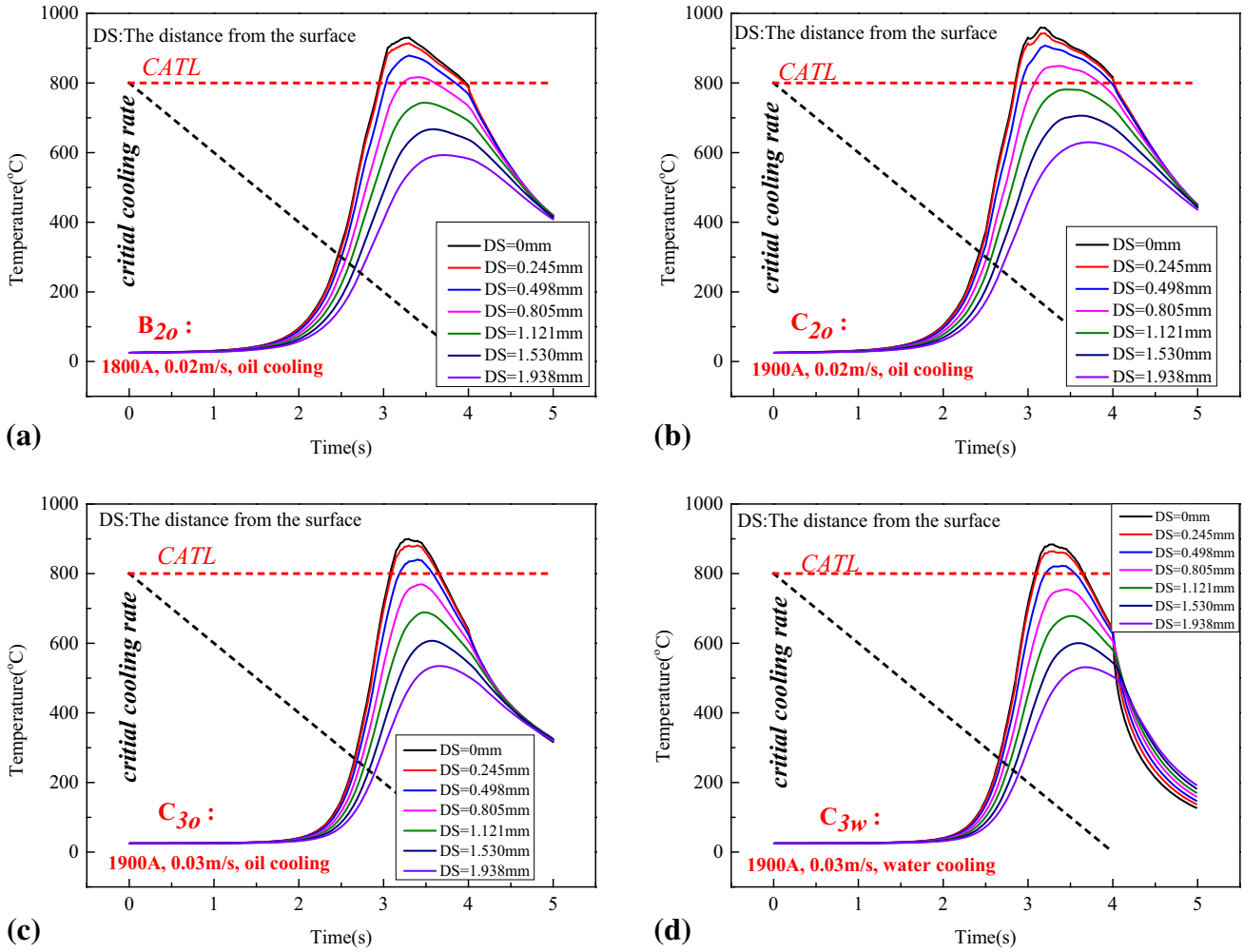

Fig. 9 The temperature-time curves of points along *Z*-axis under point P3

Table 4 Process parameters of induction hardening

Quenching medium	Frequency, KHz	Current, A	Velocity, m/s	Final time, s
Water	30	1800	0.02	9

Figure 10 shows the temperature distributions of top surface at different times during SCIH process. It can be seen that the high temperature region always appears below inductor and the highest temperature points (*H*, *I*, *J*, and *K*) always appears some place where the middle point of inductor has already pass over. This is the heating delay phenomenon as mentioned above. As the water quenching is loaded after 3 s, the "Tail" shape appears on the temperature cloud pictures at 4, 6, and 8 s, respectively.

From Fig. 10, it can be seen that the highest temperature always appears in the middle line of workpiece. The points on the top surface of the middle line of workpiece were chosen as observation points in the condition of B_{2w} and the temperature-time curves of these points are shown in Fig. 11. As mentioned above, the point P0 is the start point of the SCIH process and the point P8 is the end point of SCIH process. Therefore, the temperature-time curves of these two points are different from others. Besides, the water cooling load begins at 3 s in simulation, so the cooling process of P1 is also different from other points. It can be seen that the shape of temperature-time curves of points P2 to P7 are nearly the same and the heating process and cooling process of SCIH become stable after 2 s. The temperature development of any point of P2 to P7 is like this: the temperature increases with induction approaching and reaches the highest temperature and then decreases with induction going away from this point; the cooling rate is low first for the internal heat conduction and thermal convection of surface air but becomes large after water loading. The highest temperature and cooling rate of stable condition is about 924 °C and 1060 °C/s, which can meet the two criteria for gaining the 100% martensite microstructure in the simulation.

4.2 Microstructure and Hardness Analysis

In order to investigate the relationship between microstructure and the micro-hardness of SCIH process, the cross section of the workpiece was chosen as the analysis object to show the prediction of the micro-hardness and microstructure in the model. Figure 12(a) shows the temperature distribution in cross section, which is perpendicular to inductor moving direction when the point P4 reaching its highest temperature. It can be seen that the temperature distribution is symmetrical about the

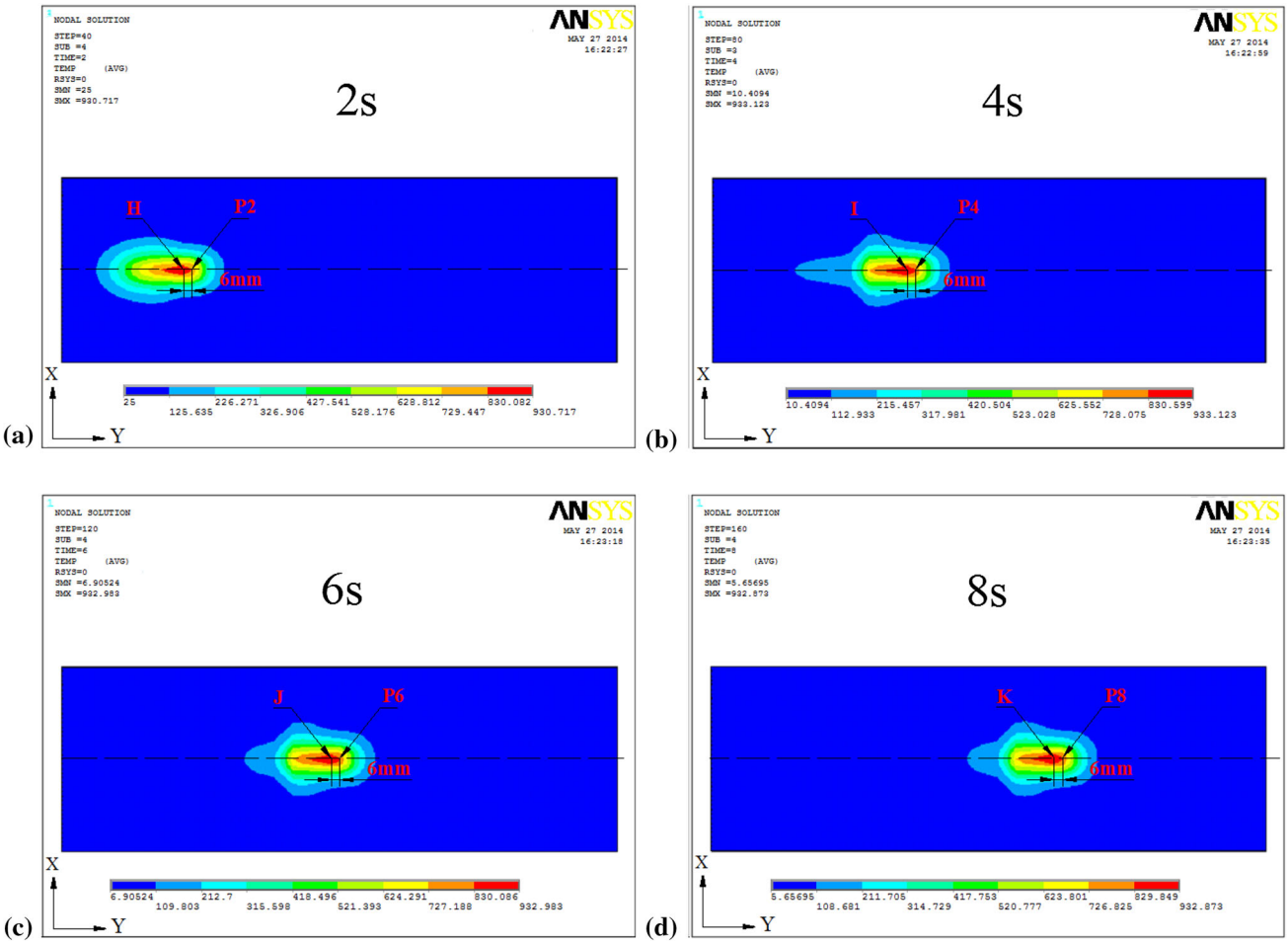

Fig. 10 The temperature distribution of top surface obtained from the FE model at different times: (a) t = 2 s, (b) t = 4 s, (c) t = 6 s and (d) t = 8 s (H, I, J and K represent the highest temperature points)

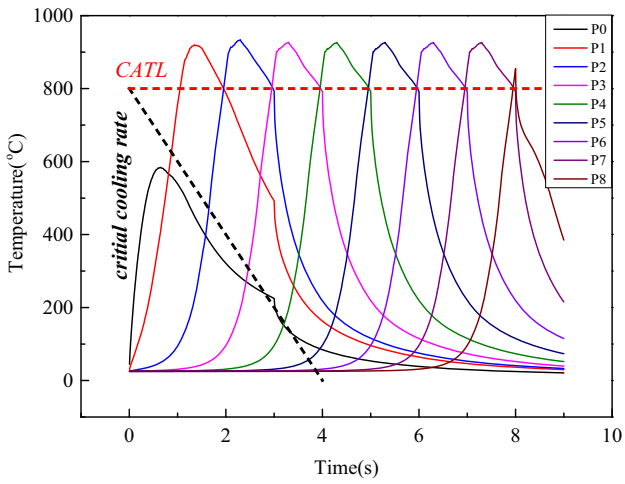

Fig. 11 Temperature-time curves of selected points on the surface

center line (L_1) of the cross section. The intersection point of the line L_1 and the top surface is selected as the point A. The other observation points named B to F are selected on the surface along the X-direction with interval distance of 1.25 mm. Figure 12(b) shows the temperature-time curves of points A to F. It can be seen that the highest temperature decreases with the increment of the distance from the line (L_1). Specifically, the temperature decreases sharply in the near region of line L_1 on the surface and decreases gently far away from line L_1. The highest temperature of Point C (DL = 2.5 mm) is about 840 °C, and the highest temperature of Point D (DL = 3.75 mm) is about 773 °C. As mentioned in section 4.1, it is reasonable to assume the temperature distribution is linear from center to margin. Therefore, 800 °C should appear at the point between point C and Point D with DL = 3.25 mm. As the cooling rates of all the chosen points on the surface are higher than the critical cooling rate of martensitic transformation (200 °C/s) with water quenching medium, the maximum width of 100% martensitic microstructure is about 6.5 mm according to the simulated result. Figure 12(c) shows the temperature-time curves of nodes in Z direction (in depth). It can be seen that the highest temperature decreases with depth increasing. In the depth of 0.805 mm, the highest temperature is about 808 °C, and in the depth of 1.121 mm, the highest temperature is about 732 °C. It is also reasonable to estimate the 800 °C appears at the point in the depth of 0.84 mm. In Fig. 12(c), it also can be seen the cooling rates of all the chosen points in depth are higher than 200 °C/s with water quenching, so the maximum depth of 100% martensitic microstructure is about 0.84 mm according to the simulated result.

Figure 13(a) and (b) shows the simulated microstructure distribution and mirco-hardeness distribution in the cross

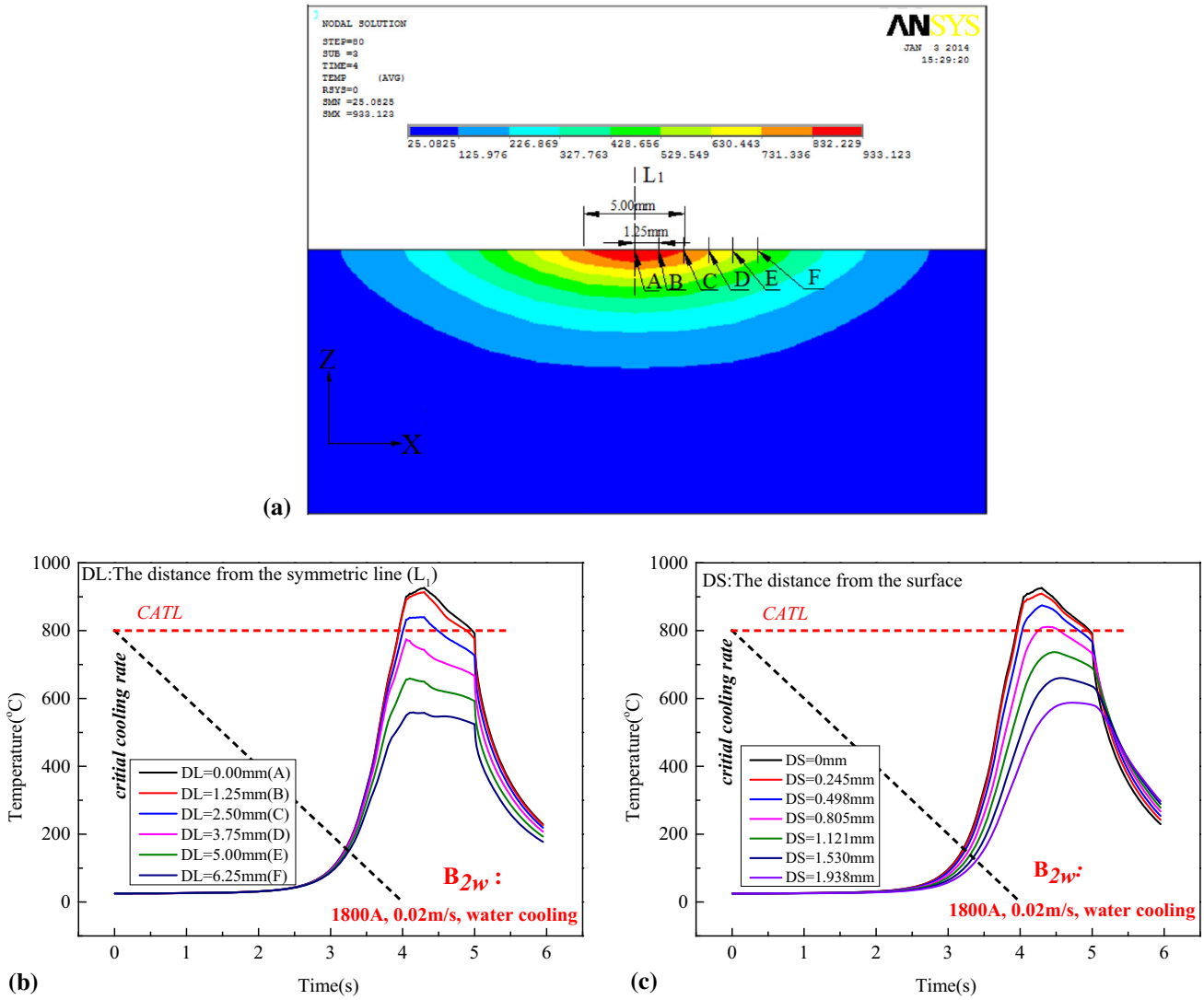

Fig. 12 (a) Temperature distribution in cross section, (b) The temperature-time curves of nodes on the top surface along *X*-axis, (c) The temperature-time curves of nodes along *Z*-axis under point P4

section of treated workpiece. From Fig. 13(a), it can be seen that the hardened region in the cross section is a crescent shape, which is also verified by the experimental cross-section metallography shown in Fig. 14(a). This phenomenon is due to the maximum heat power always appearing just below the inductor moving route in SCIH process. The maximum depth and the maximum width of 100% martensitic microstructure are about 0.84 and 6.5 mm, respectively. As mentioned before, the width of the single coil is 10 mm and the width of the magnetizer is 20 mm, which is larger than 6.5 mm. This phenomenon represents the single-coil inductor with the magnetizer can harden the area which is less than their own width. There is no transitional area between 100% martensite region and pearlite matrix region in simulated result, which is due to no consideration about the austenitizing time and the initial austenite transformation temperature (AC1) in SCIH model. Figure 14(a) shows the experimental microstructure distribution in the cross section of treated workpiece, and Fig. 14(b) is the schematic diagram of the microstructure. From Fig. 14(a) and (b), it can be seen that the maximum width of phase transitional structure along the *X*-axis is about 7.2 mm and the maximum depth along the *Z*-axis is about 1.15 mm. The maximum depth and the maximum width of 100% martensite zone are about 6.0 and 0.85 mm, respectively. By comparing the experimental and simulated results, it can be seen that the simulated error of the maximum width and the maximum depth are about 8.3 and −1.2%, respectively, in the 100% martensite region. This deviation is due to the coarse mesh in the model and no consideration of complete austenitizing time.

It is well known that there are three kinds of region in induction hardened specimen including the hardened region, transitional region, and matrix region. From Fig. 14(a) and (b), it can be seen these three regions appear in order from the surface to the core as well as from the heating center to the heating margin.

In order to obtain the detail microstructure in these three regions, different zones were chosen for metallographic

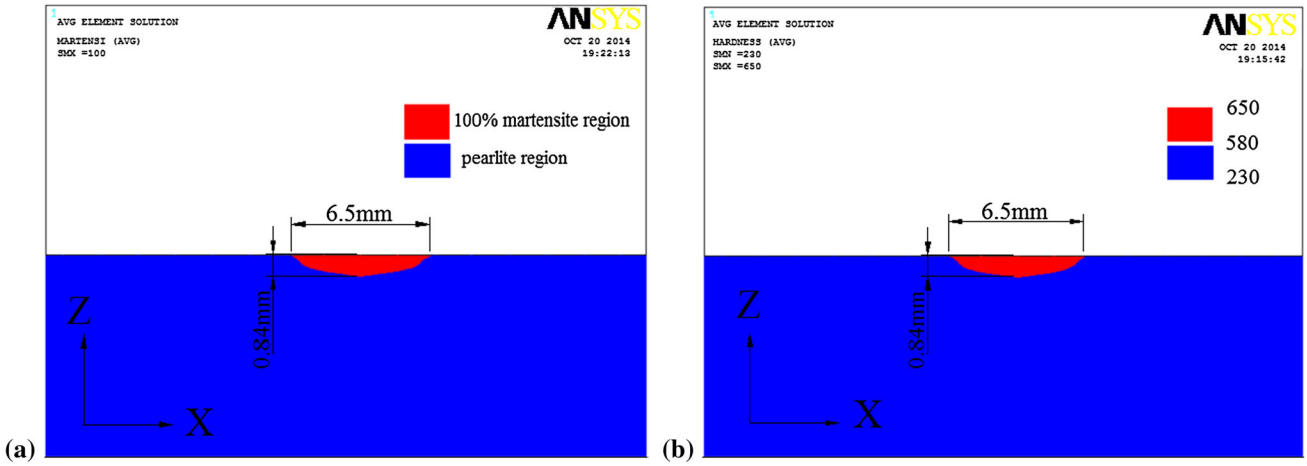

Fig. 13 (a) Simulated martensite distribution of cross section, (b) Simulated micro-hardness distribution of cross section

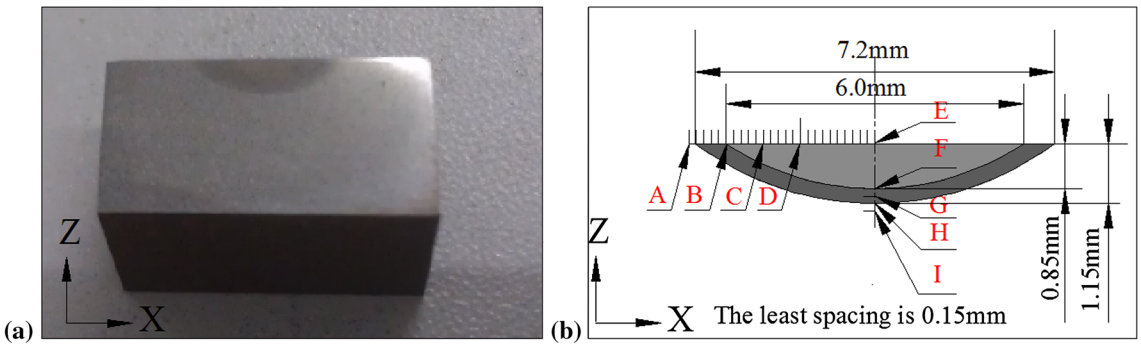

Fig. 14 (a) Metallographic specimen, (b) The selection principle of observation points for metallographic analysis

analysis. Figure 15 shows the metallographic images of the hardened, transitional, and matrix areas after SCIH treatment. It is clear that the typical pearlite appears in point *A* and point *I*, whose metallographic image shows in Fig. 15(a) and (i). The regions of point *B*, *F*, *G*, and *H* belong to the transitional zone. From Fig. 15(b), (f), (g), and (h), it can be seen the mixture of lath martensite and pearlite. Figure 15(c-e) shows the metallographic phase of point *C*, point *D*, and point *E*. All these three regions are 100% martensite. Specifically, the coarse martensite exists in point *E* and the relative refined martensite exists in point *C* and point *D*. This phenomenon is due to the growth of austenite grain during SCIH process. Compared with point *C* and point *D*, the heating temperature of point E is higher and the heating time above complete austenitizing temperature is longer, which cause the coarse martensite formation when workpiece cools with large cooling rate.

In order to verify the accuracy prediction of micro-hardness via SCIH model, the micro-hardness measurements were carried out on the polished cross section of treated workpiece using HUAYIN HV-1000 with 2 N and a diamond indenter. The measured points are from the top surface to the core region at the middle line, and the first point is in the depth of 0.15 mm. The interval distance between the adjacent chosen points is 0.1 mm. Micro-hardness measurement was carried out 3 times in each depth, and the average micro-hardness values were obtained.

Figure 16 shows the simulated and experimental micro-hardness depth profiles. From the experimental micro-hardness value in depth, it can be seen that there are three regions in treated workpiece including hardened region, transitional region, and matrix region. The hardened region (100% martensite) is from top surface to the depth of 0.85 mm. The transitional region is from the depth of 0.85 to 1.15 mm. The matrix region is from the depth of 1.15 mm to the core. The experimental micro-hardness decreases gently in hardened region, decreases drastically in transitional region, and decreases gently again in matrix region. The numerical results agree well with the experimental results in hardened region. The percentage of austenite transformation in the transitional region is not considered in this model. Therefore, the phase composition and micro-hardness value in the transitional region cannot obtain after SCIH process. The original micro-hardness value of workpiece in the numerical micro-hardness analysis is set as 230HV. The maximum errors of micro-hardness value in hardened region are about 11%, which is due to not considering the austenitizing time and the influence of grain size on micro-hardness in SCIH model.

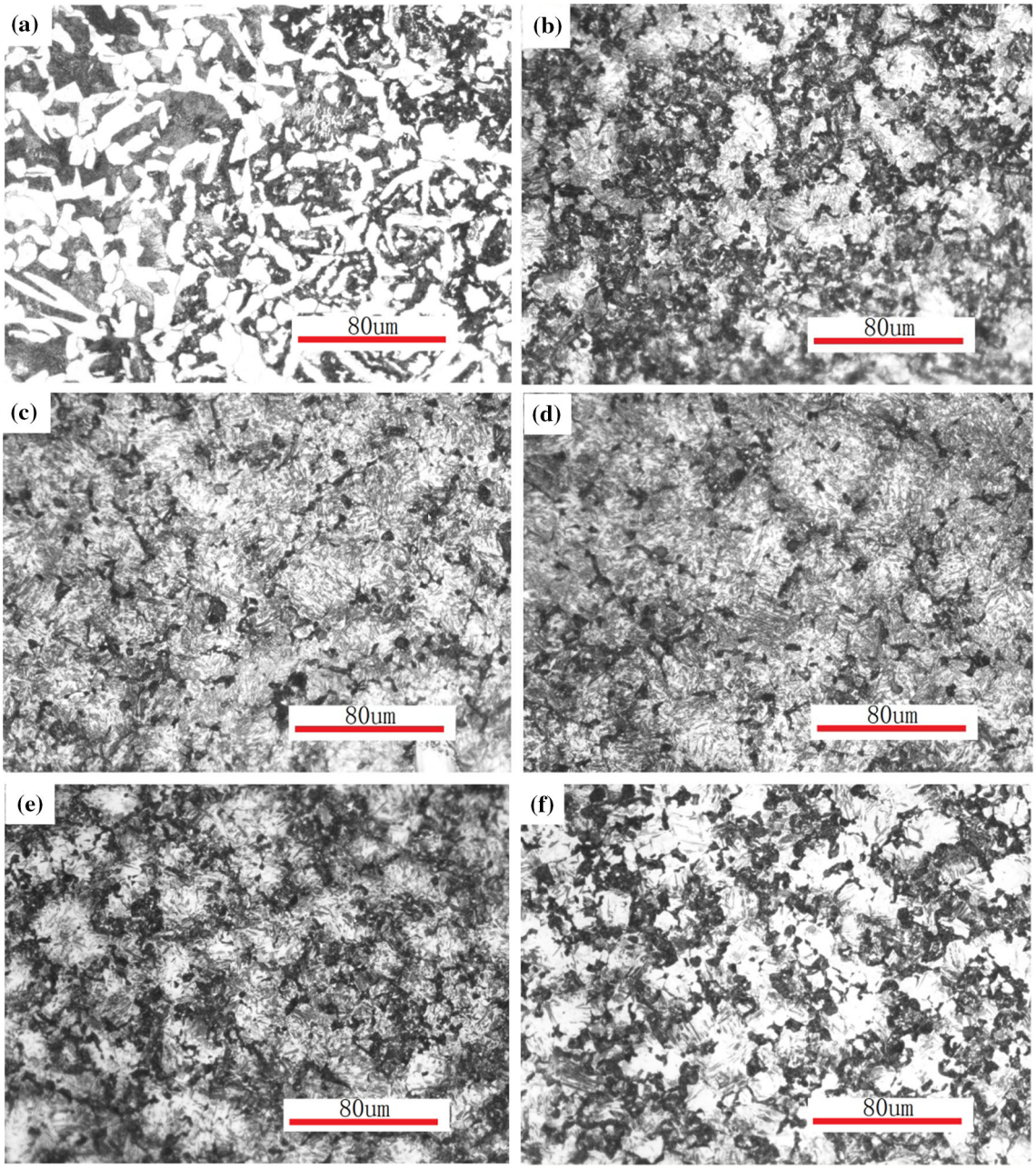

Fig. 15 The metallographic images in the cross section after SCIH treatment. (a) Point *A*, (b) Point *B*, (c) Point *C*, (d) Point *D*, (e) Point *E*. (f) Point *F*, (g) Point *G*, (h) Point *H*, (i) Point *I*

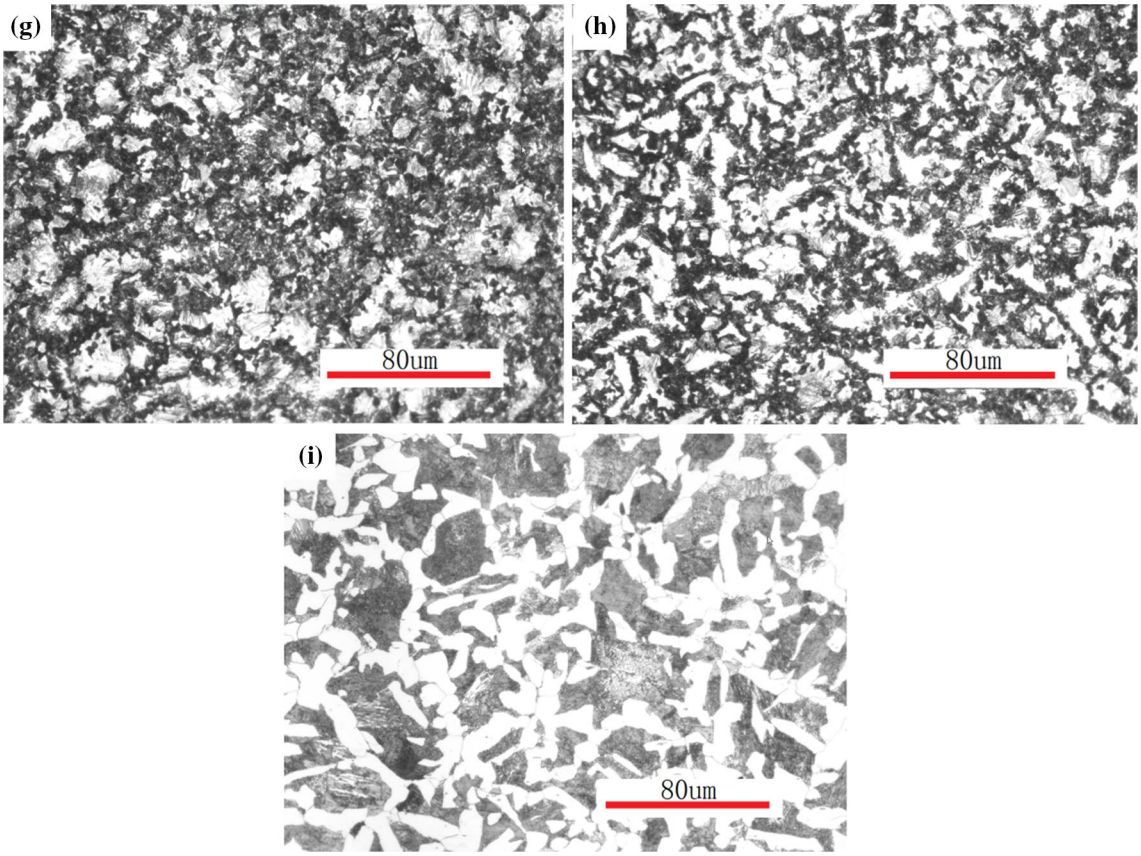

Fig. 15 continued

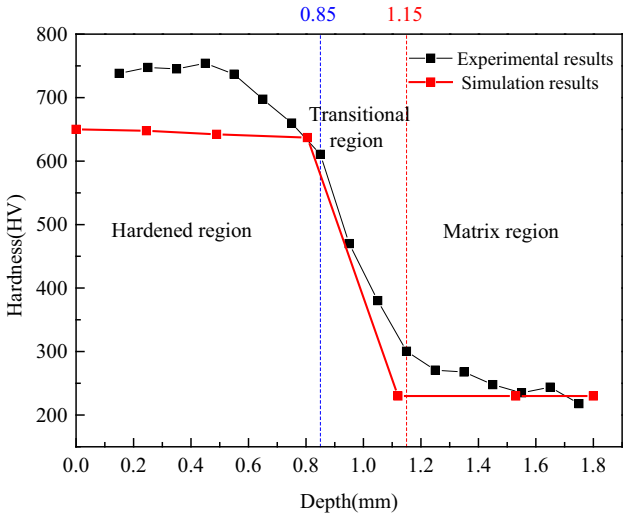

Fig. 16 The simulated and experimental micro-hardness depth profiles

5. Conclusions

A 3D finite element model to simulate the spot continual induction hardening (SCIH) process was built, and the SCIH experimental device was set up in this paper with the aim of investigating this non-stationary and transverse flux induction hardening treatment. The influence of inductor velocity, input current, and quenching medium on temperature was estimated via the SCIH model, and the simulated microstructure and micro-hardness were validated by experimental verification. The following conclusions have been reached:

(1) The cooling rate in SCIH was determined by input current, inductor velocity, and quenching medium. The heating rate and the highest temperature become larger with the increasing of input current under the same inductor velocity. The influence of input current on the highest temperature becomes more obvious with the increasing of velocity. In order to obtain martensite microstructure on surface, relatively large cooling rate is needed in the condition of relatively low input current and velocity.

(2) The heating delay phenomenon appears in all continual induction heating conditions. Furthermore, this phenomenon becomes more obvious in the condition of relatively low input current (1700 A) and relatively high inductor velocity (0.03 m/s).

(3) The simulated error of the maximum width and depth in the 100% martensite region are about 8.3 and −1.2%, respectively, which is mainly due to the coarse mesh in the model. Meanwhile, the maximum errors of micro-hardness value in 100% martensite region is about 11%, which is due to not considering the austenitizing time and the influence of grain size on micro-hardness in SCIH model.

(4) This paper simulated the phase transformation and micro-hardness distribution according to the two criteria of martensite transformation of AISI 1045 steel, but the percentage of austenite transformation in the transitional

region is not considered. That will be improved in the further study.

Acknowledgments

The financial support of the National Natural Science Foundation of China (NSFC) (No. 51175392), the Key Projects of Hubei Province Science & Technology Pillar Program (No. 2014BAA012), and the Fundamental Research Funds for the Central Universities under Grant No. 2012-IV-067 and No. 2013-VII-020 are gratefully acknowledged. The authors are grateful to all the staff of Hubei Key Laboratory of Advanced Technology for Automotive Components for supporting this work.

References

1. L.R. Egan and E.P. Furlani, A computer simulation of an induction heating system, *IEEE Trans. Magn.*, 1991, **27**, p 4343–4354
2. E.J. Davies, *Conduction and Induction Heating*, Peter Peregrinus, London, 1990
3. H. Chen, X.P. Qin, Z. Wang, and K. Gao, Numerical analysis in couple physical fields of 3D spot induction hardening, *China Surf. Eng.*, 2013, **26**, p 79–85 (**in Chinese**)
4. K. Gao, X.P. Qin, Z. Wang, H. Chen, S.X. Zhu, Y.L. Liu, and Y. Song, Numerical and experimental analysis of 3D spot induction hardening of AISI, 1045 steel, *J. Mater. Process. Technol.*, 2014, **214**, p 2425–2433
5. X.G. Yang, Transverse Flux Induction Heating and its Optimization Problem, Dissertation, Hebei University of Technology, China, 2004 (**in Chinese**)
6. V. Rudnev, D. Loveless, R. Cook, and M. Black, *Handbook of Induction Heating*, Marcel Dekker, Portland, 2003
7. V. Rudnev and D. Loveless, 12.15-Induction hardening: technology, process design, and computer modeling, *Compr. Mater. Process.*, 2014, **12**, p 489–580
8. J. Montalvo-Urquizo, Q. Liu, and A. Schmidt, Simulation of quenching involved in induction hardening including mechanical effects, *Comput. Mater. Sci.*, 2013, **79**, p 639–649
9. I. Magnabosco, P. Ferro, A. Tiziani, and F. Bonollo, Induction heat treatment of a ISO C45 steel bar: experimental and numerical analysis, *Comput. Mater. Sci.*, 2006, **35**, p 98–106
10. I. Doležel, J. Barglik, and B. Ulrych, Continual induction hardening of axi-symmetric bodies, *J. Mater. Process. Technol.*, 2005, **161**, p 269–275
11. P. Karban and M. Donátová, Continual induction hardening of steel bodies, *Math. Comput. Simul.*, 2010, **80**, p 1771–1782
12. J.A. Stratton, *Electromagnetic Theory*, McGraw-Hill, New York, 1941
13. S. Lee, E.J. Pavlina, and C.J. Van Tyne, Kinetics modeling of austenite decomposition for an end-quenched 1045 steel, *Mater. Sci. Eng.*, 2010, **527**, p 3186–3194
14. J.X. Wu, G.Y. Zhou, and L.M. Xun, *The application technology of steel hardenability*, China Machine Press, Beijing, 1994 (in Chinese)